HAL
open science

Long-term dynamics of rockslides and damage propagation inferred from mechanical modeling

Pascal Lacroix, David Amitrano

To cite this version:

Pascal Lacroix, David Amitrano. Long-term dynamics of rockslides and damage propagation inferred from mechanical modeling. Journal of Geophysical Research: Earth Surface, 2013, 118, pp.1-16. 10.1002/2013JF002766 . hal-00910379

HAL Id: hal-00910379

https://hal.science/hal-00910379v1

Submitted on 29 May 2014

HAL is a multi-disciplinary open access archive for the deposit and dissemination of scientific research documents, whether they are published or not. The documents may come from teaching and research institutions in France or abroad, or from public or private research centers.

L'archive ouverte pluridisciplinaire **HAL**, est destinée au dépôt et à la diffusion de documents scientifiques de niveau recherche, publiés ou non, émanant des établissements d'enseignement et de recherche français ou étrangers, des laboratoires publics ou privés.

Long-term dynamics of rockslides and damage propagation inferred from mechanical modeling

P. Lacroix[1] and D. Amitrano[1]

Received 15 February 2013; revised 27 September 2013; accepted 8 October 2013.

[1] Long-term observations of large active rockslides show accelerating deformation over many thousands of years since the last deglaciation. The effect of deglaciation on slope stability is however poorly understood due to (1) limited long-term observations and (2) a complex interaction between glacier retreat and hydrogeological, mechanical, and morphological processes. To assess the sensitivity of rockslide dynamics to these different processes, a model of progressive damage through intact rock mass is developed in this study, based on the finite element method. This model uses time-to-failure laws based on rock laboratory creep experiments. It is able to reproduce progressive damage localization along shear bands associated with strain rate acceleration as observed during tertiary creep. The model reproduces the different phases of deformation associated with morphologies typical of large rockslides. This model is thus suitable for simulating the dynamics of large rockslides and the transition from initiation to rapid sliding. The sensitivity of rockslide kinematics and morphology to different mechanical properties is analyzed. This analysis shows that the time evolution of the rockslide can be inferred with the knowledge of only one time parameter, independent of the knowledge of the mechanical properties of the rock mass. This parameter is here chosen as the time when the summit slope displacement has reached 10 m, a parameter that can be estimated with cosmogenic dating. The model is then used to study the effects of deglaciation on the valley flank stability and the formation of large rockslides. This study shows that the deglaciation velocity can affect the morphology of the rockslide, with the shear band of the rockslide emerging at higher elevation as the velocity decreases. We also show that the response to the deglaciation can last several thousands of years after the glacier retreat.

Citation: Lacroix, P., and D. Amitrano (2013), Long-term dynamics of rockslides and damage propagation inferred from mechanical modeling, *J. Geophys. Res. Earth Surf.*, *118*, doi:10.1002/2013JF002766.

1. Introduction

[2] The risk associated with large rockslides is of major concern in many mountainous regions. These rockslides can develop into debris flows or dam valleys; such dams create the risk of outburst floods [*Eisbacher*, 1984]. Large active rockslides with typical volumes of 1.10^7 m^3 or more are observed in many different lithological settings, in particular, in overdeepened glaciated valleys [*Erismann and Abele*, 2001]. Many of these rockslides, often associated with deep-seated gravitational slope deformation, are characterized by slow surface deformation (10 mm/yr) and long-term evolution (up to 15,000 years) [*Le Roux et al.*, 2009]. Their initiation and failure has long been thought to be a direct cause of deglaciations [*Abele*, 1974]. However, it has been shown that the rockslide evolution results from a complex combination of geological [e.g., *Brideau et al.*, 2009] and topographical factors [e.g., *Varnes et al.*, 1989], with possible interaction with external factors such as water infiltration [e.g., *Ballantyne*, 2002], seismic shaking [e.g., *McCalpin*, 1999], fluvial erosion [e.g., *Crosta and Zanchi*, 2000], or postglacial debutressing of the valley flank [e.g., *Agliardi et al.*, 2001]. All these processes act at different time and spatial scales, and their coupling is difficult to quantify. For instance, *Strozzi et al.* [2010] showed a progressive acceleration of an alpine rockslide that can be related to a combination of stress release due to deglaciation and rain events. Seasonal fluctuations of this movement illustrate the complexity of the interaction between precipitation and glacier retreat impact. This complexity means that accurate prediction of the slope failure is very challenging.

[3] The short- to medium-term (day to decennial) behavior of large rockslides is well documented, showing the important control of precipitation on the observed kinematics [e.g., *Crosta and Agliardi*, 2003; *Potherat and Effendiantz*, 2009; *Helmstetter and Garambois*, 2010; *Strozzi et al.*, 2010; *Nishii and Matsuoka*, 2010]. On a longer

[1]ISTerre, IRD, CNRS, OSUG, Université de Grenoble, Grenoble, France.

Corresponding author: P. Lacroix, ISTerre, IRD, CNRS, OSUG, Université de Grenoble, 1381 rue de la piscine, 38400 Saint Martin d'Hères, France. (pascal.lacroix@ujf-grenoble.fr)

©2013. American Geophysical Union. All Rights Reserved.
2169-9003/13/10.1002/2013JF002766

time scale (10^2-10^4 years), rockslide behavior is much less known. On such time scales, deglaciation is considered as the main activation factor of these instabilities. *Ballantyne and Stone* [2004] showed the potential long time response (several thousands of years) of rockslides to glacier retreat using cosmogenic dating of rockslide failures. The works of *Ballantyne* [2002] and *Cruden and Hu* [1993] suggested that the response of rock slopes to glacier retreat is characterized by a decreasing occurrence of rockfalls since deglaciation with a relaxation time scale of 10 to 1000 years. Another study [*Ambrosi and Crosta*, 2006] compared the present rate of deformation measured by permanent scatterer interferometry to long-term deformation rates deduced by field observations. They concluded that present-day displacement rates could explain the total observed displacements along major landslide structures without large changes since deglaciation. The long-term kinematics of two large rockslides have also been estimated using geomorphological observations and cosmogenic dating [*El Bedoui et al.*, 2009; *Le Roux et al.*, 2009]. They are characterized by slow displacement rates for thousands of years followed by a stage of progressive acceleration. In both cases, the phase of acceleration takes place several thousand years after the deglaciation. The progressive nature of the movement call into question the factors involved in their mechanics and the processes leading to their potential failure. In this context, it is of primary importance to understand the generic relations between rockslide dynamics (namely the progressive damage of a rockslope and its resulting deformation) and the role of lithology, topography, glacier retreat, and fluid flows. In this study, we aim at quantifying the effects of mechanical and geometrical parameters on the time to failure and shape of deformation of large rockslides and characterizing the time response of the rock mass to the glacier retreat.

[4] Due to limited observations on long-term rockslide dynamics, past studies have focused on the mechanical modeling of these instabilities. Different models have been developed to simulate the morphology of rockslides [e.g., *Vengeon et al.*, 1999; *Muller and Martel*, 2000; *Forlati et al.*, 2001; *Bruckl and Parotidis*, 2001; *Bachmann et al.*, 2004; *Eberhardt et al.*, 2004; *Helmstetter et al.*, 2004; *Ambrosi and Crosta*, 2006; *Stead et al.*, 2006; *Chemenda et al.*, 2009; *Kveldsvik et al.*, 2009; *Guglielmi and Cappa*, 2010]. In the event of a rockslide occurring along a preexisting surface, its mechanics can be simulated through the sliding block model [*Newmark*, 1965] based on limit equilibrium techniques. This model simulates the displacement of a homogeneous block sliding on a slope based on friction laws, but is only adapted for relatively small landslides. In larger rockslides, a preexisting sliding surface is unlikely [*Einstein et al.*, 1983], and the role of progressive failure through intact rock mass is key to explaining the initiation and the mechanics of landslides [*Muller and Martel*, 2000; *Forlati et al.*, 2001; *Eberhardt et al.*, 2004; *Bruckl and Parotidis*, 2005; *Petley et al.*, 2005; *Stead et al.*, 2006]. The initiation and progressive maturation of failure surfaces in rockslides without preexisting heterogeneities can be explained through subcritical crack growth [*Bruckl and Parotidis*, 2001]. This mechanism explains how a crack can slowly propagate even when the applied stress is much lower than the instantaneous material strength [e.g., *Atkinson*, 1984; *Brantut et al.*, 2013]. This process has been shown to be the dominant mechanism of deformation under upper crustal conditions [*Anderson and Grew*, 1977]. Other mechanisms like weathering processes can also alter rock properties. The latter however mostly concerns shallow areas ($\leq$ 50 cm) and previously damaged zones. Weathering cannot therefore explain the initiation and maturation of faults and consequently are not considered in this study.

[5] To overcome the limited application of the sliding block model to the simulation of large active rockslides, three numerical approaches have been used to model their mechanics (see *Stead et al.* [2006] and *Van Asch et al.* [2007] for a review). (1) Continuum methods (finite elements and finite differences) are based on strain-stress relationships including either progressive rock damage or strain softening, or viscosity [e.g., *Bruckl and Parotidis*, 2001]. (2) Discontinuum mechanics (distinct elements) explicitly describe the movement and the interaction between blocks through contact and friction rules [e.g., *Vengeon et al.*, 1999; *Kveldsvik et al.*, 2009]. (3) Hybrid methods use a combination of continuum and discontinuum methods to simulate the progressive brittle fracturing through adaptive remeshing techniques depending on the damaged state of the elements [e.g., *Eberhardt et al.*, 2004].

[6] Discontinuum methods are particularly suitable for modeling large displacements due to slip and can be mostly used to study the short-term landslide dynamics during the phase prior to the failure. The description of all microcracks and their propagation in the discontinuum approach is difficult to realize core complex objects like landslides, and these methods are thus not suitable to simulate progressive rock damage. Continuum methods, on the other hand, have been shown to be useful for simulating long-term dynamics and progressive rock failure [*Bruckl and Parotidis*, 2005], by the use of material of equivalent elastic properties during the rock damage evolution. These models can be used to relate processes from the initiation to the observable deformation and structures of landslides.

[7] In continuum models, progressive landslide failure is classically modeled through increasing damage and changes of progressive mechanical properties [*Forlati et al.*, 2001; *Eberhardt et al.*, 2004; *Bruckl and Parotidis*, 2005; *Bachmann et al.*, 2009; *Chemenda et al.*, 2009; *Guglielmi and Cappa*, 2010]. In these models, damage occurs in zones where a stress field criterion (usually Mohr-Coulomb or Hoek-Brown criterion) has been reached. Damaged elements are simulated using analogue materials of lower shear modulus or lower mechanical resistance (friction and/or cohesion variations). However, time is not well accounted for in these models. *Bruckl and Parotidis* [2005] simulated time by fitting observed landslide velocity during primary and tertiary creep regimes, corresponding respectively to phases of damage zone maturation and acceleration toward the slope failure. The time was thus not directly related to the damage evolution and to the mechanical properties of rocks. This limitation prevents the use of these models for studying the time control of long-term effects like glacier retreat. The originality of our approach is to include time-to-failure laws, derived from subcritical cracking instead of empirical laws used in previous studies, to simulate the long-term behavior of rock slopes. We show that this single process reproduces many temporal and spatial features of large rockslides.

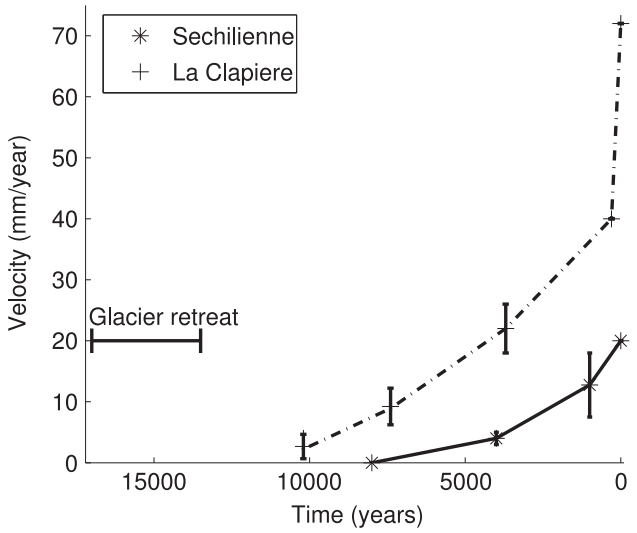

Figure 1. Velocity of the Séchilienne and the La Clapiere landslides estimated from cosmogenic dating for past velocities [*Le Roux et al.*, 2009; *El Bedoui et al.*, 2009] and geodetic measurements for actual velocities [*Kasperski*, 2008; *El Bedoui et al.*, 2009].

[8] The paper is organized as followed. We first review the large similarities between the long-term dynamics of rockslides and laboratory creep experiments (section 2). These similarities allow us to transpose a model of progressive damage of rocks under brittle creep [*Amitrano and Helmstetter*, 2006] to large rockslides (section 3). The model uses time-to-failure laws based on laboratory rock creep experiments. We show that the model is suitable for simulating the kinematics and damage of large rockslides and the transition from the initiation to rapid sliding (sections 4.1 and 4.2). Then, we analyze the sensitivity of the landslide dynamics to different mechanical properties (section 4.3). Finally, this model is used to study the impact of glacial retreat on the geometry and time to failure of large rockslides (section 5).

2. Long-Term Rockslide Dynamics Observations

[9] The long-term evolution of landslides is known from morphological observations and dating of their scarps [*Le Roux et al.*, 2009], cracks opening [*El Bedoui et al.*, 2009], debris [*Hippolyte et al.*, 2009], or deposits [*Gutiérrez-Santolalla et al.*, 2005]. A precise dating sequence has notably been carried out in two alpine rockslides, in Séchilienne [*Le Roux et al.*, 2009] and La Clapiere [*El Bedoui et al.*, 2009], using cosmic ray exposure dating. These two sequences show the landslide evolution over 15,000 years, that is, since the last deglaciation (Figure 1). They show different phases: (i) no significant displacement is observed during several thousand years. (ii) Then a slow and progressive increase of displacement rate occurs. The associated deformation initiates from the toe and propagates to the top of the slope. (iii) A rapid acceleration and failure of the slope can then occur.

[10] The stress release resulting from the deglaciation or "glacial debutressing" has been frequently proposed to explain the initiation of slope movements [e.g., *Cossart et al.*, 2008]. The deformation onset was sometimes observed to be synchronous with deglaciation [*Agliardi et al.*, 2009]. However, the large time lapse between deglaciation and initiation of the slope movement observed in the Séchilienne and La Clapiere rockslide sequences questions the real triggering factor of these rockslides. Time lapses of several thousand years were also often reported between deglaciation and slope failure in many other landslides mostly in the Alps (Flims landslide [*Ivy-Ochs et al.*, 2009], Fernpass rockslide [*Prager et al.*, 2009], Koefels landslide [*Ivy-Ochs et al.*, 1998], and Kandertal landslide [*Tinner et al.*, 2005]). These studies provided exposure ages during the Holocene when conditions were warmer and wetter, and corroborated the hypothesis of climatic triggering to explain the origin of the failure [*Soldati et al.*, 2004]. Seismic triggering has also been invoked to explain these dates in the Alps, as ages of gravitational destabilizations coincide with the tectonic activities [*Sanchez et al.*, 2010].

[11] However, the cases of Séchilienne and La Clapiere bring new insights into the long-term dynamics of large rockslides, showing the large time scale of rock damage processes. In these two cases the climatic factor cannot explain the progressive acceleration observed over more than 8000 years. An alternative explanation could rise from the progressive acceleration being related to damage evolution of the rock mass. The different phases observed correspond first to maturation of the failure surface without significant displacement, followed by a phase of progressive acceleration until the slope fails. These phases coincide with different creep regimes observed during rock sample creep experiments [*Boukharov et al.*, 1995; *Brantut et al.*, 2013]. The primary phase of creep is characterized by strain rate decrease and is followed by a tertiary creep regime where strain rate and velocity increase. The velocity is notably found to follow a power law that has been used to predict the failure [*Voight*, 1989]. The secondary creep regime observed in brittle creep experiments [*Brantut et al.*, 2013], corresponding to the transition between these two phases, is sometimes observed in nature [*Heap et al.*, 2011]. Previous studies have shown that there is a progressive change from primary to tertiary creep, experimentally [e.g., *Heap et al.*, 2009b; *Brantut et al.*, 2013], numerically [*Amitrano and Helmstetter*, 2006], and analytically [*Main*, 2000]. Secondary creep can be considered as the transition between these two steps, when the strain rate varies very slightly. Based on these observations and also as already shown by a previous study [*El Bedoui et al.*, 2009], rockslide dynamics and creep experiments share large similarities. Due to these similarities, the model proposed in this study for damage evolution and rockslide dynamics is transposed from a model of brittle creep on rock samples [*Amitrano and Helmstetter*, 2006].

3. Modeling

3.1. Progressive Damage Model

[12] The common approach to simulate the progressive failure of brittle rock is to adopt an elastic-brittle-plastic or strain-softening model. This approach is often based on a linear Mohr-Coulomb failure criterion or on a nonlinear criterion such as the Hoek-Brown failure criterion, above which either the elastic properties (Young's modulus and/or

Poisson's ratio) of the rock sample [e.g., *Amitrano and Helmstetter*, 2006] or material strength [*Chemenda et al.*, 2009] vary. *Hajiabdolmajid et al.* [2002] developed a model of progressive rock failure based on the cohesion loss and friction increase as plastic strain increases. This model has been used to simulate the relief evolution at a regional scale [*Guglielmi and Cappa*, 2010].

[13] A major problem, however, arises from the use of the model developed by *Hajiabdolmajid et al.* [2002] to simulate the landslide dynamics. This model relies on the hypothesis that the strength of the material decreases first by friction reduction and then by cohesion reduction using an ad hoc time function. This makes it difficult to relate the time to failure to material properties when rock strength changes. On the contrary, the elastic-brittle model simulates progressive damage of rocks through changes in elastic properties, without changing their strength. In particular, *Amitrano and Helmstetter* [2006] simulated the time evolution of brittle rock damage using time-to-failure laws based on creep experiments and subcritical crack growth theory [*Atkinson*, 1984]. This model reproduces both the spatial distribution of the damage at the macroscopic scale and its temporal evolution.

[14] Hereafter, we provide a short description of this model. More details can be found in *Amitrano and Helmstetter* [2006]. The model is based on time-to-failure laws in order to model the time evolution of damage and deformation under creep. A macroscopic element i is characterized by its Young's modulus E_i. An element is damaged when the shear stress τ on this element exceeds a damage threshold. Experimental observations by *Heap et al.* [2009a] showed that the damage onset can be described by the Mohr-Coulomb criterion. This criterion is thus chosen as the instantaneous damage threshold. The Mohr-Coulomb criterion is classically defined by the cohesion C and the internal friction angle Φ relating normal (σ) and shear stress (τ):

$$\tau = C + \sigma \tan(\Phi) \tag{1}$$

[15] This damage process is simulated through the decrease in elastic properties of the element i by a factor D ($0 < D < 1$):

$$E_{i,t+\Delta t} = (1 - D)E_{i,t} \tag{2}$$

[16] When the instantaneous threshold is not fulfilled, i.e., when the applied stress is lower than the instantaneous strength, we consider a delayed damage described by a static fatigue law. The increment of time Δt needed to reach the delayed damage is based on measurements of time to failure (t_f) from static fatigue law experiments, which express t_f as a function of the major stress σ_1 and the instantaneous strength σ_0:

$$t_f \sim T_0 \exp(-b\sigma_1/\sigma_0) \tag{3}$$

The time T_0 has been shown to be dependent on the parameter b as $T_0 \sim \exp(b)$ [*Amitrano and Helmstetter*, 2006]. Equation (3) expresses the brittle fracture of rocks through subcritical crack growth. This process is related to an environmentally sensitive chemical reaction between silicate bond and water [*Atkinson*, 1987]. In rocks, the parameter b has been shown to decrease with increasing humidity [*Nara et al.*, 2010], increasing temperature [*Kranz et al.*, 1982], decreasing confining pressure [*Atkinson*, 1987], and increasing degree of anisotropy of the crystal orientation fabric [*Sano and Kudo*, 1992]. The range of b parameter variation is derived from creep experiments on rock samples (see the review in *Amitrano and Helmstetter* [2006] for more details). For a typical rockslide, temperature, pressure, and the crystal orientation fabric vary little over time. Therefore, the main variations of b are caused by water circulation. We do not however consider here the effect of water.

[17] The decrease of Young's modulus in the element i leads to the redistribution of stresses around this element, which can allow other elements to exceed the threshold of the yield stress criterion. This process creates an avalanche of events, typical of many failure phenomena [*Zapperi et al.*, 1997; *Sethna et al.*, 2001]. At the end of the avalanche, the stress state of each element is recalculated and the process is iterated until no other element exceeds its damage threshold.

[18] Elastic interactions between elements and the heterogeneity of the mechanical properties lead to the emergence of a complex macroscopic behavior. The elementary ruptures connect until they form a macroscopic shear band as damage rate starts accelerating, which corresponds to the onset of the tertiary creep. The model also reproduces the power law decay of the rate of strain, damage events, and energy release associated with the primary creep regime. The tertiary creep is also well simulated, with an increase of these three parameters. The model thus reproduces many properties of rock creep as observed at the laboratory scale, including both the macroscopic behavior as also simulated by micromechanical models [*Brantut et al.*, 2012] and the progressive damage localization. These two observations have not been captured acting in concert by previous modeling efforts. In particular, an increase of the apparent Poisson's ratio is observed at the macroscopic scale [*Amitrano*, 1999], despite the Poisson's ratio ν being kept constant at the elementary scale during the damage process. This type of simple model is characterized by the emergence of macroscopic properties that are not included at the elementary scale [*Amitrano*, 2004], including the anisotropic nature of the damage at the macroscale despite the Poisson's ratio being considered as a scalar. Moreover, from the experimental point of view, previous studies [*Katz and Reches*, 2004] have shown that the scalar representation of damage at the local scale does not preclude the good representation of the anisotropic damage at the macroscopic scale. More elaborated theoretical models considering tensorial expression of the damage could be used instead, but their inherent complexity and the several parameters needed preclude, at least at this stage of our work, their application to study the temporal evolution of damage within a rock slope.

[19] It is however well known from experiments that the Poisson's ratio evolves during the deformation of rocks. The manner in which the Poisson's ratio evolves varies depending on the type of rock. Theoretical considerations suggest that the Poisson's ratio decreases in the same manner as the Young's modulus [*Kemeny and Cook*, 1986; *Kachanov*, 1993]. Experimentally, however, the general case is that ν increases from an initial value of about 0.25–0.35 to a higher value sometimes as high as 0.45–0.5. This is particularly the case of initially low porosity rocks [see *Heap et al.*, 2010; *Eslami et al.*, 2010]. The range of increase of ν when the macrofailure is achieved may vary from 0.05 to 0.15. For initially porous rocks, the evolution of ν can be

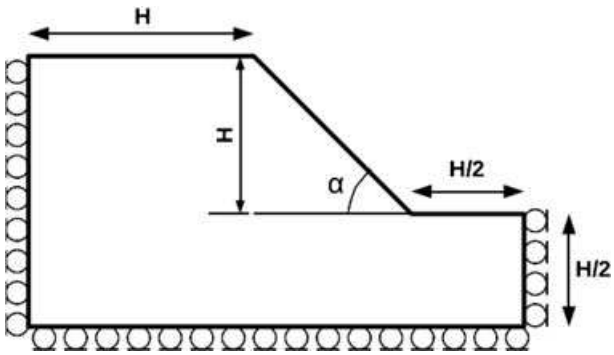

Figure 2. Schematic diagram showing parameters related to model geometry and boundary conditions.

more complicated as a decrease can been observed for some rocks [e.g., *Wassermann et al.*, 2009; *Heap et al.*, 2010]. These relationships have been established for uniaxial loading conditions, and it is unsure that they also apply for triaxially loaded rocks. As a consequence, including the evolution of ν in our model at the elementary scale appears to be difficult due to the variety of possible evolutions and the dependence on the type of rock. In this work, we chose to keep ν stable. The detail behavior related to a more elaborated evolution of the damage is beyond the scope of the present study.

3.2. Large Rock Slopes Modeling

[20] The aforementioned model is adapted to simulate rock slope behavior under the influence of gravity. The geometry is controlled by the angle α of the slope (Figure 2). Typical values of α for large rockslides range from 25° to 50° [*McCleary et al.*, 1978]. The height of the slope is fixed to typical values of 1000 m [*McCleary et al.*, 1978]. The distances to the slope boundaries are defined in Figure 2 and are chosen long enough to avoid interactions with the damaged zone. The domain is divided into triangular elements. The meshing uses a Delaunay triangulation. The input of the triangulation, referred in the following as the mesh resolution, is the maximum edge size of the triangles. The triangulation is then computed by optimizing the quality of the elements, which is a criteria on the triangle area distribution.

[21] The mesh resolution has been chosen based on two criteria. First for optimizing the simulation duration and second for describing with sufficient details the geometry of the failure. We tested the effect of the size of the mesh elements with three different values: 100 m, 50 m, and 30 m (Figure 3). The simulation time increased by approximatively 25 as the element size is divided by 2 (Table 1). Then, the geometry of the failure is found to be poorly defined with an element 100 m in size. At this scale, the simulation shows that the geometry of the modeled deformation depends on the orientation of the borders of the individual elements. Geometry of the failure plane can even be determined by the arrangement of the elements. On the contrary, the simulations with elements 50 m and 30 m in size provide a very similar geometry of the failure: the parabolic shape of the failure plane is conserved as well as its double branch on top of the slope (Figure 3). Based on these simulations, we chose a mesh element 50 m in size (approximatively 3700 elements for a 45° slope), meaning that we consider the material as homogenous at this scale.

Table 1. Simulation Duration for Various Mesh Resolution[a]

Mesh Resolution	Number of Elements	Simulation Duration
100 m	1,000	200 s
50 m	3,700	5,000 s
30 m	10,400	45,000 s

[a]The geometry of the simulations is shown in Figure 3.

[22] The mechanical properties of rocks at the rockslide scale are derived from the properties at the rock sample scale. Unfortunately, few measurements have been realized to determine the mechanical parameters of rocks and rock masses at a macroscopic scale. Some attempts have been made to characterize the macroscopic values of rock strength and deformability from field observations, notably using the Geological Strength Index (GSI) [*Hoek and Brown*, 1998]. This index can be related to elastic modulus, cohesion, and friction [*Cai et al.*, 2004]. Despite all its limitations (the GSI is a local, superficial, subjective measurement, which is not adapted to anisotropic materials and sensitive to ground water content), it provides a range of the macroscopic mechanical properties of rocks that show scaling effects between the laboratory sample scale and the macroscopic scale. This scaling effect can partly be explained by the fact that mechanical properties at the laboratory scale are measured on fairly intact rock samples, whereas large fractures in the rock mass are encountered at larger scales in observations. This damage size effect has been modeled [e.g., *Min and Jing*, 2003] and sometimes measured [*Kulatilake et al.*, 2004]. These different studies showed that

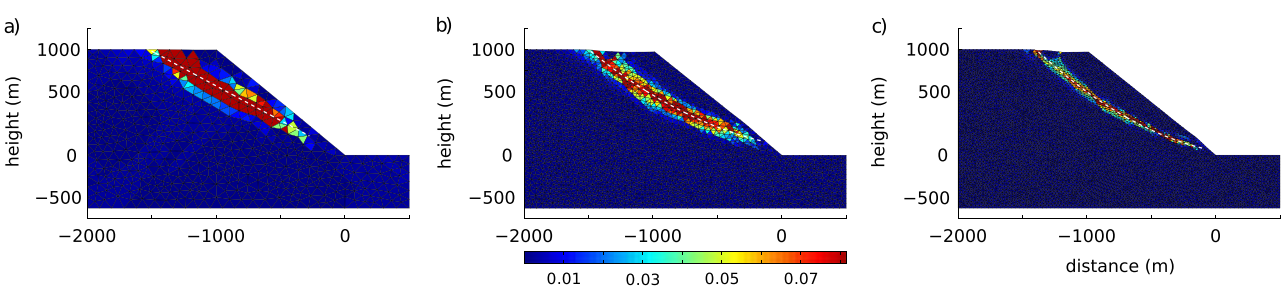

Figure 3. Simulations realized for the same set of parameters but with three different mesh resolutions. Size of the elements are (a) 100 m, (b) 50 m, and (c) 30 m. The white dashed line is the best fit for the failure plane (see section 4.3.2).

Table 2. Mechanical Parameters Used in the Simulations

Parameter	Definition	Min Value	Max Value	Steps
α	Slope angle	25°	50°	5°
Φ	Internal friction	25°	40°	
μ	tan (Φ)	0.5	0.8	0.1
ν	Poisson's ratio	0.35	0.45	0.05
C_0	Minimum cohesion	8 MPa	20 MPa	3
b	Coefficient	20	40	5
$E_{i,t}$	Initial Young's modulus	20,000 MPa	20,000 MPa	
D	Damage coefficient	0.1	0.1	

(i) the cohesion of rocks at macroscopic scale is lower than measured on rock samples, (ii) the Young's modulus is lower at the rock mass scale than at the rock sample scale, and (iii) the Poisson's ratio increases with increased damage and is thus related to the observation scale. The Poisson's ratio is found to increase by 20% when increasing the size of observation from a 10 m scale to a 30 m scale [*Kulatilake et al.*, 2004], reaching 0.34 at a 30 m scale. Contrary to the scaling effects described above, friction is found to be fairly constant at greater scales [*Ishida et al.*, 2010].

[23] Based on this scaling effect, we define the range of variation of the mechanical parameters used in the following as shown in Table 2. The range of variation of parameters is chosen to represent a large range of material properties. The Poisson's ratio is voluntarily chosen high to take into account both the scaling effect and the generally higher ν when damage evolves (see section 3.1).

[24] The simulation starts with the following boundary conditions (Figure 2). (i) The cohesion values are randomized to create heterogeneities on the mesh and enable the initiation of the process. For simplicity reasons, cohesion values are chosen following a uniform distribution between C_0 and $2C_0$, where the range of variation of C_0 is defined in Table 2. This randomization has very little effect on the simulations as shown later. (ii) The bottom boundary is fixed in the vertical direction, and the left and right boundaries are fixed in the horizontal direction. This means that at the time scale of the simulations, the tectonic displacement can be neglected. (iii) Roller boundary conditions are used in the other directions (free displacement along the horizontal direction for the bottom boundary and free displacement along the vertical direction for the lateral boundaries). These conditions are classically used for simulating the elastic reaction of the embedding material [*Griffiths and Lane*, 1999; *Forlati et al.*, 2001; *Guglielmi and Cappa*, 2010], as it allows the reduction of the impact of boundary conditions when large scales are simulated [*Guglielmi and Cappa*, 2010]. (iv) Gravity is applied to each node. The stress is calculated using a rock density of ρ = 2700 kg m^{-3}, corresponding to fairly common values for rocks.

[25] During the simulation, three kinds of parameters are estimated. (i) The displacement field of each node of the mesh. In the following, we will particularly focus on the summit slope displacement (d_s), as shown in Figure 4a. (ii) The number of ruptures in each element. This parameter evolution is represented in Figure 5 at different times of the simulation. (iii) We also define N, the cumulative number of ruptures over all the elements, as shown in Figure 4b. The simulations are run until d_s reaches 200 m. Once this threshold is exceeded, the continuous material hypothesis cannot be considered true anymore (20% of deformation). According to experimental observations at the end of the dynamic failure, the simulations diverge when the material is softened because the loading is kept constant. We therefore chose to stop the simulations once N reaches 100,000. This value has been chosen because in our simulations, the tertiary creep is always found to occur beforehand.

4. Results and Discussion

[26] There are 450 simulations which have been performed using different mechanical parameters (Table 2) on slopes without preexisting heterogeneities, in order to test the sensitivity of the model. Hereafter, we present the generic behavior and the effect of each parameter.

4.1. Space and Time Analysis

[27] All the simulations exhibit similar overall evolution over time (Figure 4) and space (Figure 5), that is, (i) the cumulative number of ruptures presents first a decelerating followed by an accelerating pattern. (ii) The time evolution shows a progressive acceleration of d_s. (iii) The ruptured elements are first located at the toe and propagate upward. This evolution creates a damaged zone, from where a shear band

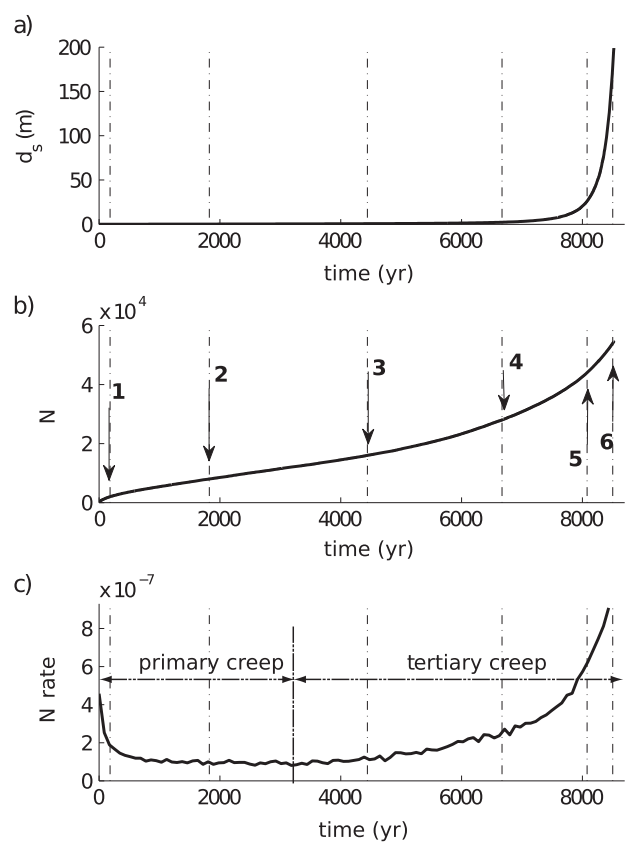

Figure 4. Example of time evolution of (a) summit displacement d_s, (b) Cumulative number of ruptures (N), and (c) rate of N as a function of time. The set of parameters represented here is (ν = 0.40, μ = 0.6, C = 8 Mpa, b = 30). Primary and tertiary creep regimes are defined upon the simultaneous decrease and increase of the N rate. The arrows show the times of the different steps represented in Figure 5.

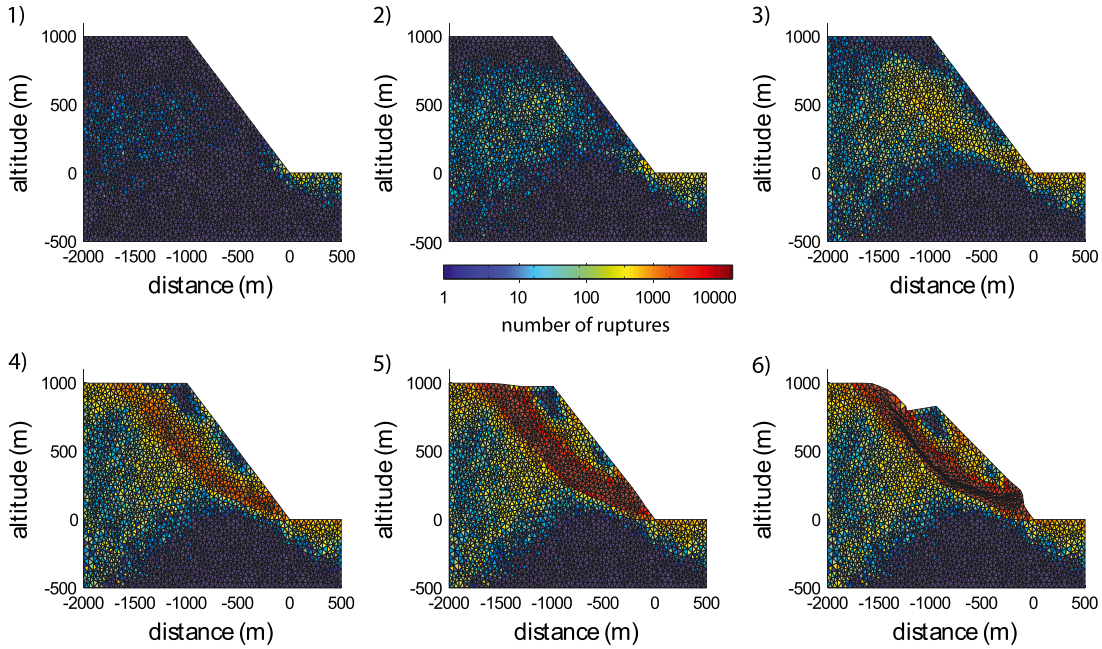

Figure 5. Different steps (Figure 4) of the damage evolution process. The color scale represents the number of damage events per element in logarithmic scale. The set of parameters is (ν = 0.40, μ = 0.6, C = 8 Mpa, b = 30).

progressively emerges. This shear band is firstly located at the top of the damaged zone and propagates downward. This progressive localization leads to the emergence of a highly damaged zone that we consider as the failure surface. (iv) Displacements are small over a large time span, and we define the time t_{10} when d_s = 10 m, or 1 % of the height of the slope.

[28] The simulations correctly reproduce the long-term dynamics of large rockslides (section 2) with progressive acceleration of the deformation. The modeling clearly displays a two-stage damage process: first, an initiation and maturation of the damaged zone with diffuse damage and without much displacement, and second, a stage of acceleration when the damaged area connects the toe and the top of the slope. These two stages coincide with the primary and tertiary creep regimes observed in rock creep experiments characterized by, respectively, a decrease and an increase in the number of ruptures and strain rates (Figure 4c). We must notice that the randomization of the cohesion at the initiation of the simulation leads to very similar results over time, with 1% error over both t_{10} and N_{10}. This value has been calculated by running the model 20 times for the same set of mechanical parameters but with different cohesion randomizations.

[29] The modeling also reproduces the general morphology of large rockslides, with a scarp at the top of the slope and bulging at its toe [*Agliardi et al.*, 2001]. The spatial randomization of the cohesion does not affect this general

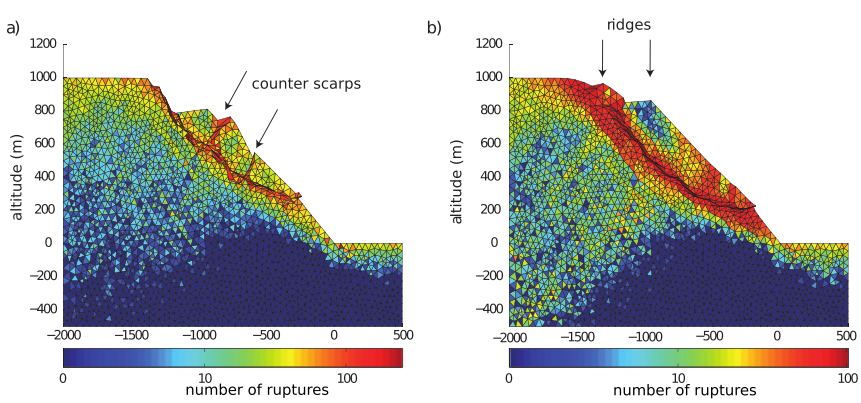

Figure 6. Example of final morphology for two simulations with different sets of parameters. (left) Obtained for ν = 0.35, μ = 0.8, C = 20 MPa, b = 20. (right) Obtained for ν = 0.35, μ = 0.6, C = 11 MPa, b = 20. The color scale represents the cumulative number of ruptures per element at the end of the simulation. These simulations exhibit commonly observed features of large rockslides like counter scarps or double ridges.

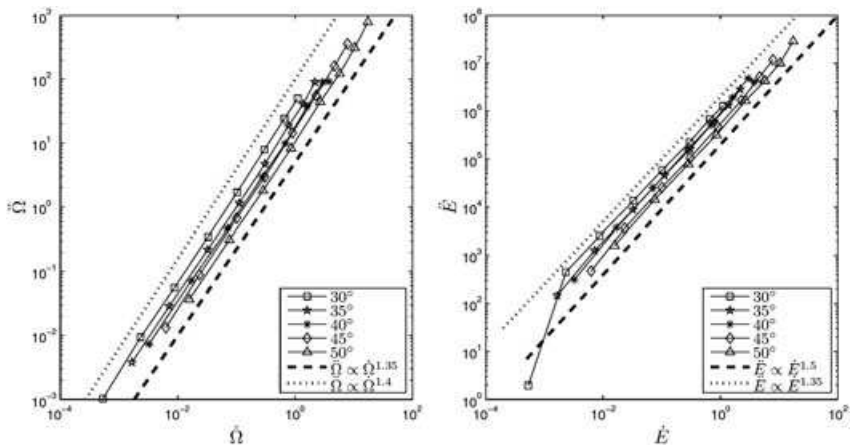

Figure 7. Relationship between the first and the second time derivative of the summit displacement ($\dot{\Omega}$ and $\ddot{\Omega}$) in the subplot a) and of the energy released ($\dot{E}$ and $\ddot{E}$) in the subplot b). Dashed lines indicate the Voight law with $\gamma = 1.35$ and $\gamma = 1.4$ for the displacement and $\gamma = 1.35$ and $\gamma = 1.5$ for the energy which corresponds to the best fits of the data.

morphology. The randomization only affects the details of the shear band. For instance, it can lead to the formation of specific features once the shear band is formed, like double ridges or counter scarps (Figure 6). These morphologies are usually observed on large rock slope instabilities [e.g., *Agliardi et al.*, 2001]. We conclude that double ridges or counter scarps of rockslides can be created during the deformation process and can be related to heterogeneities of the mechanical properties of the rockslope. In particular, it is observed that counter scarps are associated with curvature changes of the shear band geometry (Figure 6) and thus are formed after the localization of the shear surface.

[30] We also observe that the shear band does not emerge at the toe. This behavior reproduces that of numerous large rockslides that are suspended above the valley (e.g. Rosone [*Forlati et al.*, 2001], Ruinon [*Tarchi et al.*, 2003], and Séchilienne [*Kasperski*, 2008]).

4.2. Acceleration Toward the Failure

[31] The end of the simulations shows an accelerating pattern of both displacement and the number of ruptures (Figure 4), which concurs with many observations reporting accelerating displacements or deformation rates [*Bhandari*, 1988; *Zvelebill and Moser*, 2001; *Petley et al.*, 2002] or seismic release rate [*Amitrano et al.*, 2005] before the slope failure. Depending on the authors, the acceleration is found to follow either an exponential or a power law toward the time of collapse. *Petley et al.* [2002] suggested that the exponential law is observed for landslides in ductile materials. The power law acceleration of the slope prior to the failure has been proposed to be analogous to the final stage of the tertiary creep of brittle materials as observed in lab-scale experiments [*Saito and Uezawa*, 1961; *Kennedy and Niemeyer*, 1971; *Voight*, 1989; *Heap et al.*, 2011]. Such power laws have been observed for landslides and proposed as a tool for determining either the time of collapse or velocity thresholds useful for risk assessment [*Crosta and Agliardi*, 2003]. *Voight* [1989] proposed a general law linking the acceleration and the velocity of the displacement of a creeping material toward failure:

$$\ddot{\Omega} = A\dot{\Omega}^{\gamma} \tag{4}$$

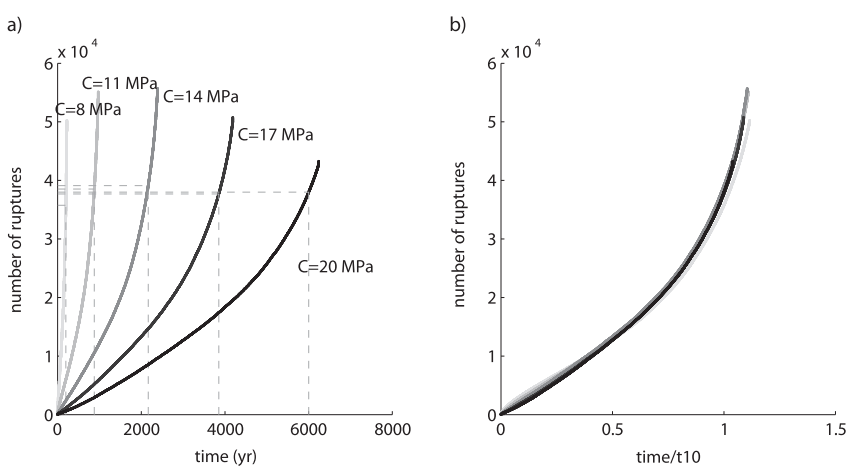

Figure 8. (a) Cumulative number of fractures (N) as a function of time for different cohesion values and $\mu = 0.7$, $b = 25$, $\nu = 0.4$. The dashed lines represent t_{10}, the times for which $d_s = 10$ m. (b) The same parameter but with the time scale normalized by t_{10}.

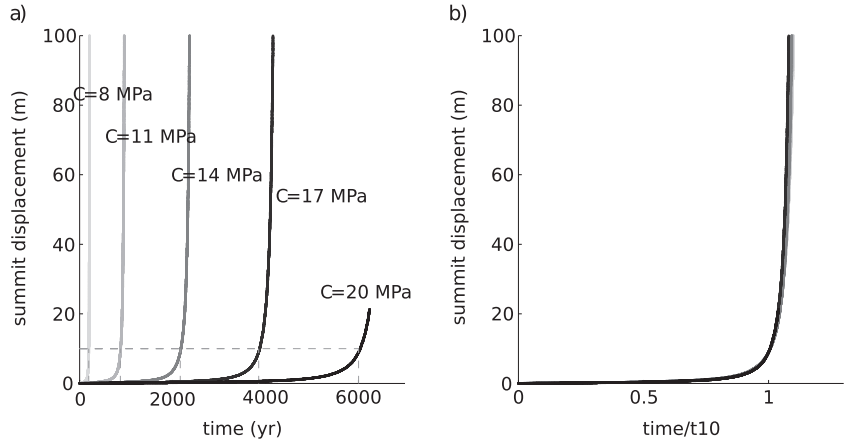

Figure 9. Same as Figure 8 but for the displacement of the slope summit (d_s).

The first and second time derivatives of the displacement are $\dot{\Omega}$ and $\ddot{\Omega}$. A and γ are constants. Voight suggests that this power law can be recovered when using various variables, including strain and seismicity rate. In the following, we analyze the acceleration generated in the model to see if it fits with Voight's model. We compute the first and second time derivative for surface displacement ($\dot{\Omega}$ and $\ddot{\Omega}$, respectively) and for the energy released ($\dot{E}$ and $\ddot{E}$, respectively) for different slope angle values while keeping all the other parameters constant (b = 25, C = 8 MPa, μ = 0.6, ν = 0.4). Figure 7 shows that this concurs with Voight's model. The best fit is obtained with γ = 1.35 – 1.4 for the displacement for all slope angles. For energy release, γ ranges from 1.5 to 1.35 as the slope angle varies from 30° to 50°. These values concur with natural observations, with values between 1.1 and 2.2 reported on various slopes [*Crosta and Agliardi*, 2003]. We should however notice that the exponent of the Voight's model calculated with the progressive damage model is nearly constant whereas the one calculated on observations varies and is dependent on the time span of observation [*Crosta and Agliardi*, 2003]. This can be explained by seasonal forcings that can affect the dynamics of natural slopes and that are not modeled here.

[32] We should also note that the final step of the simulation after which the damage localization is fully developed occurs for velocity between 1 and 17 m yr^{-1}, corresponding to 3–46 mm/day. These values are comparable to the velocity thresholds calculated by *Crosta and Agliardi* [2003] for the Ruinon rockslide, which are used as emergency/alert triggers. Hence, the proposed model appears to be adequate for describing the acceleration related to the progressive damage of a rock slope.

4.3. Sensitivity Analysis to the Mechanical Properties

[33] In this section, we analyze the 450 simulations covering the range of parameters described in Table 2.

4.3.1. Sensitivity of the Time Evolution

[34] The cumulative number of ruptures N shows a progressive increase leading to the macroscopic rupture (Figure 8a). The curve $N(t)$ shows homothetic behavior, that is, the number of ruptures for different mechanical parameters can be inferred by a transformation of the time axis normalized by t_{10} (Figure 8b). This behavior shows that the cumulative number of ruptures is not significantly affected by the mechanical parameters of the slope. For the same amount of displacement, the same number of ruptures occurs. This concurs with experimental observations [*Baud and Meredith*, 1997; *Kranz and Scholz*, 1977], showing that the failure during creep occurs at a constant amount of strain and number of ruptures, independent of the applied stress.

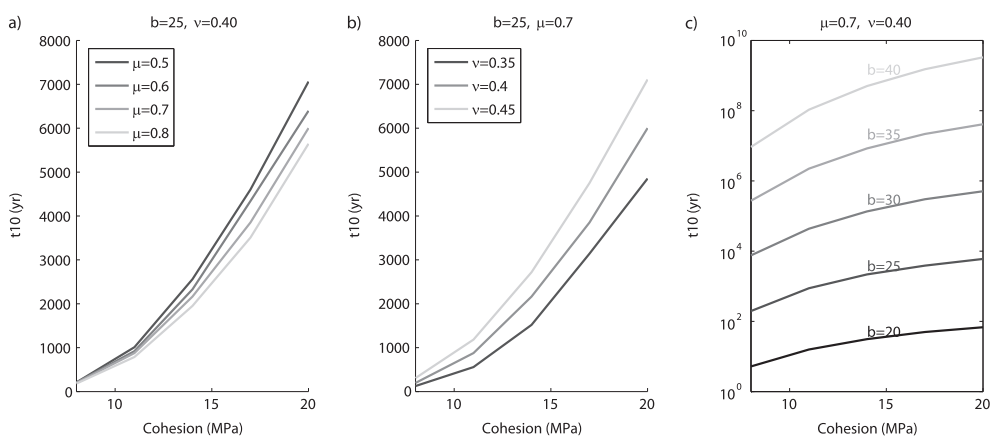

Figure 10. t_{10} (year) as a function of the cohesion represented for different values of the (a) friction, (b) Poisson's ratio, and (c) b parameter.

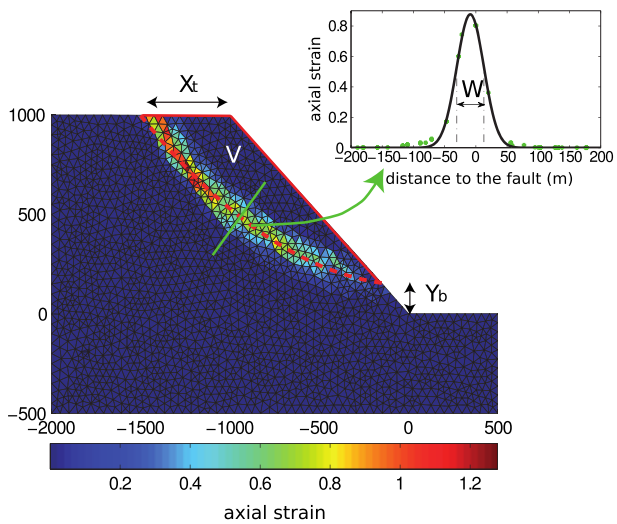

Figure 11. Definition of the different geometric parameters used in this study. V = volume, W = width of the damaged zone.

[35] The displacement d_s presents a progressive acceleration with time, strongly affected by all mechanical parameters of the slope (Figure 9). All the simulations display a long plateau followed by a rapid acceleration. The $d_s(t)$ evolution is found to be similar for all mechanical parameters once the time scale has been normalized by t_{10}. Therefore, to better quantify the impact of the mechanical parameters on this plateau length, the time t_{10} is analyzed (Figure 10). This analysis shows that t_{10} increases as C, b, and ν increase and as μ decreases. The evolution of t_{10} with b is obvious, because b controls the time to failure of rock sample elements. The effect of cohesion also concurs with observations at the rock sample scale, with increasing time to failure for stronger rocks. The effects of ν and μ are less obvious. Unfortunately, no observations, even at the rock sample scale, exist on the sensitivity of the time to failure for these mechanical parameters.

4.3.2. Sensitivity of the Morphological Evolution

[36] To better quantify the geometry of the damaged zone and its sensitivity to different mechanical parameters, we first characterize the damaged zone when the summit displacement reaches 10 m. This is done by first calculating the axial strain gradient ($\ddot{\epsilon_{xx}}$) for each element of the slope, then selecting the points with ($\ddot{\epsilon_{xx}}$) greater than ($\frac{\max(\ddot{\epsilon_{xx}})}{10}$), and finally fitting these points with a 2° polynomial (Figure 11).

[37] Based on this shear band retrieval, we then compute the different geometrical values (Figure 11):

[38] 1. The volume V of the rockslide refers to the pseudo 2-D volume between the failure surface and the free surface.

[39] 2. The thickness T of the rockslide is calculated by averaging the thicknesses over all the pseudo 3-D volume.

[40] 3. The parameter X_t corresponds to the X coordinate of the failure surface at the top of the model, with $X = 0$ at the toe.

[41] 4. The parameter Y_b corresponds to the Y- coordinate of the failure surface at the bottom of the model, with $Y = 0$ at the toe of the slope.

[42] 5. The parameter W corresponds to the width of the damaged area calculated on the axial strain values when the summit displacement reaches 10 m. To retrieve W, we first compute for every 50 m along the failure surface, the quantity ϵ_{xx} as a function of the normal distance to the failure surface d. The quantity $\epsilon_{xx}(d)$ is fitted with a Gaussian function (Figure 11). We then define w as two times the standard deviation of this Gaussian function. W is then found by averaging w along the failure surface.

[43] Parameters C, ν, and b have first-order effects on the rockslide volume and thickness (Figure 12), with a thickness decrease, while C and ν increase and b decreases. The effect of μ on the failure plane geometry is of second order. An increase of μ slightly decreases the volume and the landslide thickness. This simulated effect of μ concurs with results from numerical modeling simulating the progressive damage through cohesion loss [*Chemenda et al.*, 2009].

[44] Finally, the sensitivity of the width W of the damaged area to ν, μ, b, and C is shown in Figure 13. It shows

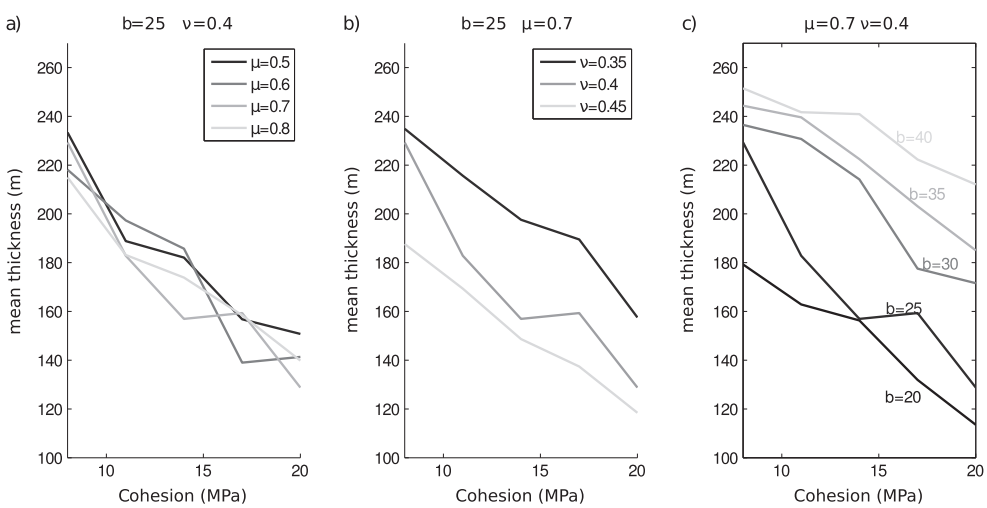

Figure 12. Mean thickness T (m) retrieved from simulations with different mechanical parameters. The coupled effect of the cohesion and (a) the friction, (b) the Poisson's ratio, and (c) the b parameter.

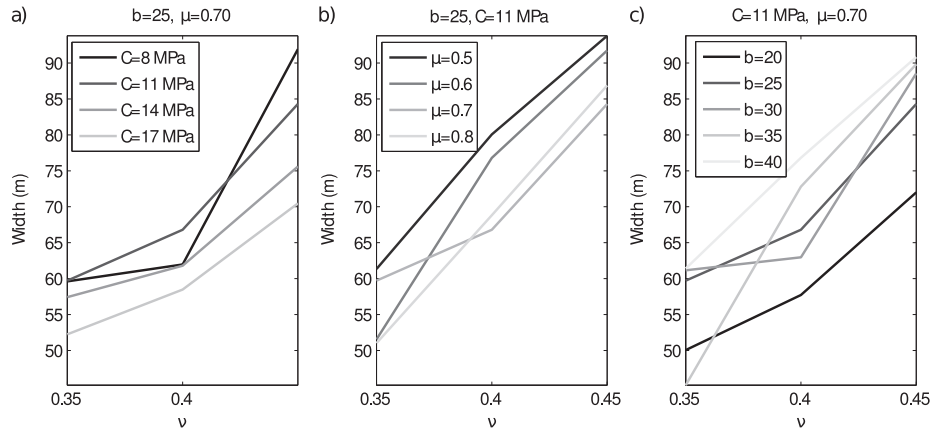

Figure 13. Effects of mechanical parameters on the width of the damaged zone (W). The coupled effect of the Poisson's ratio and (a) the cohesion, (b) the friction, (c) the b parameter.

the dominant effect of ν and the secondary effect of C, μ, and b on W. W increases as ν and b increase, and as C and μ decrease. The C, μ, and ν effects show that softer rocks have a wider damaged zone than stiffer rocks. This behavior reflects the fact that softer rocks have a more diffuse damaged zone than stiffer rocks, as usually observed experimentally or in the field [*Jaeger and Cook*, 1976].

[45] The slope modeling shows a large impact of b on the shear band geometry and particularly on the rockslide mean thickness (Figure 12). This effect is surprising as b is a time-to-failure parameter (equation (3)). This shows that the b value is a critical parameter of the simulation. The b parameter is always measured at the rock sample scale, and the scaling effect of b with the sample size is not known. Thus, for a specific case study, we propose to evaluate the b parameter by fitting the simulated t_{10} to the long-term displacement of the observed rockslide. This time can be estimated using for instance cosmogenic dating of the scarps with an uncertainty of about 5–10% [e.g., *Le Roux et al.*, 2009]. This error propagates with uncertainties of about 1% on the estimation of the b parameter.

4.3.3. Slope Effects

[46] The model has been run for different slope angles ranging from 25° to 50°, corresponding to typical values of large rockslides (Figure 14). It is first observed that simulations with slopes of 25° never evolve toward the rupture, as no localization occurs. We note that for all simulations that evolve toward rupture, 25° corresponds to the lowest-angle values of the sliding surface as it emerges at the slope toe (Figures 5, 6, 11, and 15). This can explain why simulations with a slope angle of 25° do not evolve toward the rupture. This shows either that the model is not adapted to simulate the rockslopes for slope angles equal to or below 25° or that the evolution of rockslopes of low slope angles is controlled by preexisting heterogeneities [*Brideau et al.*, 2009] (either topographical or inside the massif).

[47] We observe that the qualitative pattern of deformation does not change for various slope angles. However, the time t_{10} and the number of ruptures N_{10} to reach 10 m of displacement highly depend on the slope, that is, both t_{10} and N_{10} increase as slope angle decreases. We notably see that an exponential relation exists between α and t_{10}, and a quasi linear relation exists between t_{10} and N_{10} (Figure 14). This behavior reflects the fact that slopes of lower angles are more stable.

[48] To show the applicability of this model to simulate the time evolution of different slope morphologies, we also run the model using a different valley profile, characteristic of glacial alpine valleys (Figure 15). This profile is composed of steeper slopes at lower elevations due to erosion by glaciers and a bank at the slope toe. This simulation follows exactly the same steps as observed previously in the case of a simplified geometry (section 4.1), with an initiation of the surface rupture at its toe and a progressive maturation toward the top. The change of slope at the middle of the slope limits the propagation of the fault surface to the top of the slope. This general pattern reproduces correctly the state of strain observed on the Randa rockslide, exhibiting a similar geometry [*Eberhardt et al.*, 2004]. Concerning its time evolution, the general primary and tertiary phases are also observed as well as the progressive acceleration of the damage rate toward the rupture associated with the tertiary creep. The profile is however characterized by a longer phase of fault localization (primary creep) than a similar simulation using a constant angle profile of 35°, due both

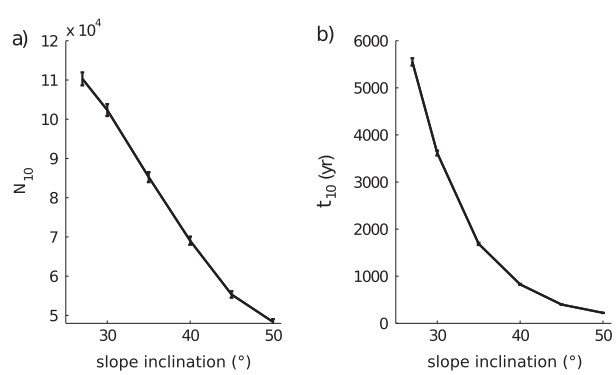

Figure 14. Evolution of parameters (a) N_{10} and (b) t_{10} as a function of the slope inclination. Set of parameters used is $\nu = 0.4$, $\mu = 0.7$, $C = 20$ MPa, and $b = 25$.

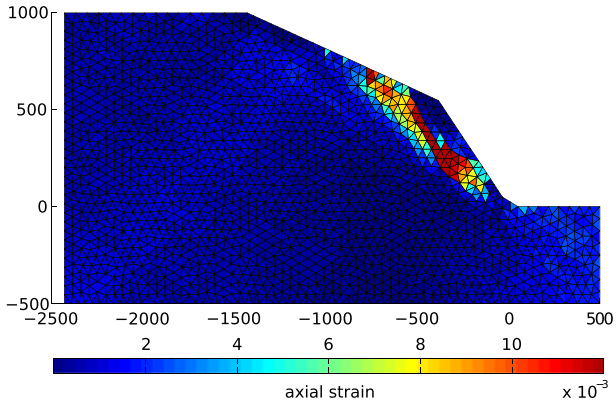

Figure 15. Axial deformation obtained over a typical topographical profile of alpine valleys. Set of parameters used is $\nu = 0.4$, $\mu = 0.7$, $C = 20$ MPa, $b = 25$.

to the presence of the bank at its toe and the lower extent of the steepest part, therefore applying a lower stress on its toe.

5. Effect of Glacier Retreat

5.1. Glacier Retreat Modeling

[49] In this part, we run the model over rock slopes affected by glacier retreat to better understand the shape and time response of the slope to the deglaciation. We assume the valley history starts as the valley is formed and completely filled by a glacier. The effect of the valley excavation by glacier or fluvial erosion is thus not taken into account in this study. The latter has been shown to have the same qualitative effects as valley deglaciation on the slope stability, that is to say a collapse of the upper part of the slope but not of the toe [*Hurlimann et al.*, 2006]. Moreover, it is known that glaciations lead to erosion of the valley walls and therefore to steeper slopes. This process is a major factor of instability (Figures 14 and 15). For these two reasons, we hypothesize that omitting the valley erosion before the glaciation will not alter the qualitative results of glacier retreat effect.

[50] We analyze two parameters of the deglaciation: the origin time of deglaciation t_0 since the glacier emergence (assumed to be the beginning of the glacial period) and the duration s to deglaciate the entire valley. In the French Alps, the last glacial period occurred during the last years of the Pleistocene from $\approx$ 110,000 to 10,000 years ago. The maximum extent of glaciation occurred $\approx$ 18,000 years ago and lasted for approximatively 5000–8000 years, with many local variations. At that time, the ice thickness reached 1200 m above sea level [*Monjuvent and Winistorfer*, 1980]. These values provide an idea of the glacier retreat duration s ($\approx 10^3$–10^4 years) compared to the time t_0 ($\approx 10^5$ years).

[51] We use a constant slope angle of 45° and a slope height of 1000 m, characteristics of alpine valleys such as the Romanche or Tinée where the Séchilienne and the La Clapière rockslides developed. The effect of the glacier is modeled as a boundary condition on the slope flanks, that is, the ice applies a pressure p on each element perpendicular to the slope, dependent on the ice column thickness (h_{ice}) the ice density $\rho_{\text{ice}} = 917$ kg.m^{-3}, and the gravity g:

$$p = \rho_{\text{ice}} g h_{\text{ice}} \tag{5}$$

Together with the boundary conditions described in section 3, p is applied to the slope. The model is run during the glacier retreat, which is assumed to be a linear function of time:

$$h_{\text{ice}} = H \quad \text{if } t \leq t_0 \tag{6}$$

$$h_{\text{ice}} = H\left(1 - \frac{t - t_0}{s}\right) \quad \text{if } t_0 + s > t > t_0 \tag{7}$$

$$h_{\text{ice}} = 0 \quad \text{if } t > t_0 + s \tag{8}$$

5.2. Glacier Retreat Effect

[52] The resulting fracturing activity and summit displacement are shown in Figure 16. We analyze the effect of t_0 and s on the morphology and time to failure of the slope for one set of mechanical parameters ($b = 28$, $C = 10$ MPa,

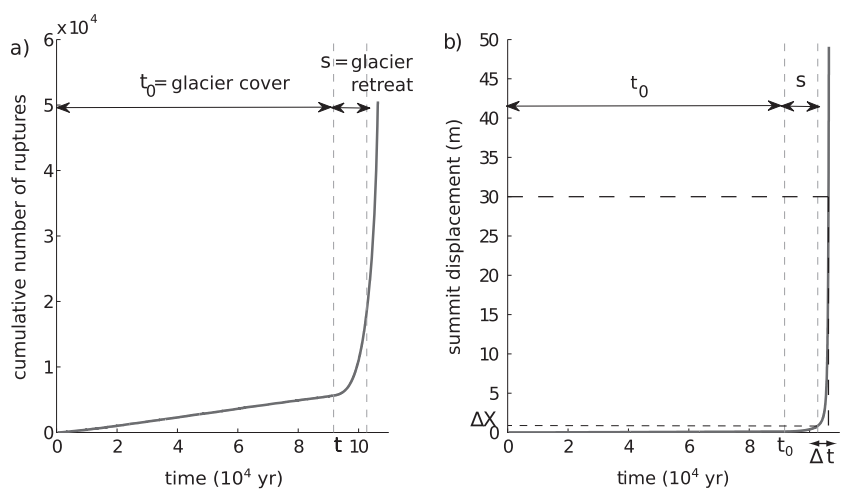

Figure 16. Cumulative number of (a) rupture events and (b) summit displacement as a function of time for a scenario where a glacier fills the valley until time t_0. Deglaciation occurs between t_0 and $t_0 + s$. The set of parameters is $b = 28$, $C = 10$ MPa, $\mu = 0.7$, $\nu = 0.4$.

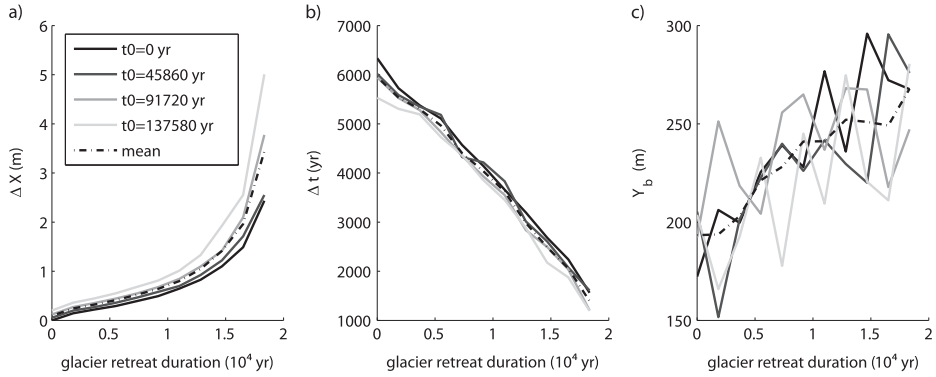

Figure 17. Effect of glacier retreat on the temporal and morphological behavior of rockslides. (a) Summit displacement at the end of deglaciation. (b) Time between the end of deglaciation and the time to reach 30 m of displacement. (c) Altitude of the failure emergence above valley bottom Y_b (Figure 11). All parameters are represented as a function of glacier retreat time span s and for different glacier retreat onset time t_0. The set of parameters is (b = 28, C = 10 MPa, μ = 0.7, ν = 0.4).

ν = 0.4, μ = 0.7). This set of parameters, notably the b parameter, has been chosen because it provides a time scale on the order of the one observed for the Séchilienne and La Clapière rockslides, for which both glacier retreat history and scarp dating are available. Three parameters are shown in Figure 17 , that is, (1) the summit displacement ΔX at the end of the deglaciation ($t = t_0 + s$), (2) the time Δt between the end of the deglaciation and the time the summit displacement reaches 30 m. This 30 m value corresponds to the height of the scarp observed on the Séchilienne rockslide [*Le Roux et al.*, 2009], and (3) the parameter Y_b corresponding to the altitude of emergence of the sliding failure plane (altitude of the toe is $Y = 0$).

[53] We see that the glacier impacts the slope behavior in different ways. First, it stabilizes the slope during the entire glaciation. The summit displacement is blocked in most cases by less than 1 m during glaciation (Figures 16 and 17). Second, its retreat leaves the movement to evolve freely with a sudden acceleration of the summit after the retreat (Figure 16). Third, the time response Δt of the movement to the glacier retreat is longer for shorter s and t_0 (Figure 17) and is on the same order of magnitude than the deglaciation duration. Finally, it changes the failure geometry, with a migration of the failure surface upward as the glacier retreat speed decreases (Figure 17). The three first points correctly reproduce the long-term kinematics observed on the La Clapière and Séchilienne rockslides (Figure 1) [*El Bedoui et al.*, 2009; *Le Roux et al.*, 2009], with first a displacement blocked during the initial phase of deglaciation and then a large time response for the movement after deglaciation (3000 years for La Clapière and 5500 years for Séchilienne). This large time response for these two rockslides can be explained by a long characteristic time (large b parameter) of the rock damage.

[54] This set of observations also show that the duration of retreat is a dominant parameter controlling the position of the damaged zone. The migration of the failure surface upward shows that the damage localization is small during the phase of glaciation and that shear band formation occurs during the phase of deglaciation. Other simulations done with much different values of b do not show an upward migration of the failure plane. This shows that the fault migration can occur only when the characteristic time of rock damage (here exp(b = 28) s $\approx$ 4500 years) is on the order of the characteristic time of the glacier retreat (s). This control of the speed of retreat on the rockslide geometry concurs with observations of different rockslides along alpine valleys [*Ambrosi and Crosta*, 2011]. Indeed, *Ambrosi and Crosta* [2011] showed that deglaciation occurs at different rates along the same alpine valley and can lead to different failure geometries at different positions along the valley.

[55] Finally, our modeling shows that the kinematic response of the slope to the glacier retreat can have occurred many thousands of years after the end of deglaciation (Figure 17) because of the long maturation time of the damage zone after deglaciation. This can lead to an onset of the movement during the climatic optimum of the Holocene, occurring between 4000 and 8000 years after the end of deglaciation. Therefore, an ambiguity between deglaciation and climate forcing can exist concerning the triggering factors of these large instabilities. This result is particularly relevant when considering that the rockslide initiation can be an indicator of climate change [e.g., *Ivy-Ochs et al.*, 1998; *Soldati et al.*, 2004]. We argue that the validity of this conclusion must be estimated by evaluating the time response of the rockslide to the glacier retreat, particularly for large rockslides where maturation of failure surfaces is a long-term process.

6. Conclusion

[56] We developed a model simulating the long-term dynamics of large rockslides based on the progressive damage of rocks. This model aims to simulate the time and geometrical evolution of large rockslides. Progressive damage is simulated by decreasing Young's modulus through time. The time evolution of elastic modulus is simulated by the use of time-to-failure laws observed at the laboratory rock scale (10^{-1}m).

[57] This model exhibits observed geomorphological and temporal features of large slow-moving rockslides. In particular, it reproduces primary and tertiary creep regimes observed on rockslides. The tertiary creep regime is found to follow Voight's law according to field observations.

Spatially, it explains how a shear band can initiate without predisposed heterogeneities, and it reproduces geomorphologic features observed on rockslides such as double ridges or counter scarps. Therefore, this model is well adapted for rockslide dynamics simulations from the initiation up to velocity thresholds in the order of 20 mm/day. After this value, discontinuum methods should be used.

[58] The sensitivity of rockslide geometry and time behavior to different mechanical properties of rocks is estimated. Our study shows the large sensitivity of rockslide dynamics to rock mass properties, particularly cohesion, Poisson's ratio, and the *b* parameter, a parameter defining the velocity of subcritical crack growth at the massif scale. All these properties are difficult to measure at the slope scale, which could make the use of this model to specific case studies difficult. However, a major result of this analysis is that the time evolution of the landslide dynamics scales with one time parameter t_{10}, reflecting a characteristic time scale of the deformation. This time evolution is also kept unchanged in shape, concurring with a constant parameter of the Voight's law. The time evolution of the landslide dynamics can thus be inferred independently to the knowledge of the mechanical properties of the slope. This parameter is chosen as it can easily be measured on head scarps of major landslides using cosmogenic dating [e.g., *Le Roux et al.*, 2009].

[59] This model can also be used to test different mechanisms leading to the present geometry and dynamics of specific rockslides. In particular, we test the deglaciation effect on the landslide kinematics and geometry. The evolution toward the rupture is obtained without introducing external factors such as rain, seismic shaking, or permafrost thaw. The deglaciation is found to have three main effects: (i) the time response of the rockslide movement to the glacier retreat can be as long as many thousands of years, (ii) the kinematic response is progressive with accelerating movement, and (iii) long deglaciation creates a migration of the rockslide upslope, which can explain different rockslide morphologies along the same valley.

[60] This modeling also questions the factors of initiation of such large instabilities, with possible response of the rockslide to the last deglaciation during the Holocene. Therefore, caution must be taken when considering the rockslides onsets as climatic proxies [e.g., *Ivy-Ochs et al.*, 1998]. For quantitative comparison of these different forcings, future developments of the model should include pore water pressure and seismic shaking effects on the rockslide dynamics.

[61] **Acknowledgments.** This work has been funded by the ANR TRIGGERLAND project. It is also a contribution to the FP6 TRIGS program. The authors thank Sarah Carson for reviewing the writing. We are also grateful to Mike Heap, Vidar Kveldsvik, and two anonymous reviewers for their thorough and detailed reviews.

References

Abele, G. (1974), *Bergsturze in den Alpen: Ihre Verbreitung, Morphologie und Folgeerscheinungen*, Dt. Alpenverein, München.

Agliardi, F., G. Crosta, and A. Zanchi (2001), Structural constraints on deep-seated slope deformation kinematics, *Eng. Geol.*, *59*(1-2), 83–102, doi:10.1016/S0013-7952(00)00066-1.

Agliardi, F., G. B. Crosta, A. Zanchi, and C. Ravazzi (2009), Onset and timing of deep-seated gravitational slope deformations in the eastern Alps, Italy, *Geomorphology*, *103*(1), 113–129, doi:10.1016/j.geomorph.2007.09.015.

Ambrosi, C., and G. B. Crosta (2006), Large sackung along major tectonic features in the Central Italian Alps, *Eng. Geol.*, *83*(1-3), 183–200, doi:10.1016/j.enggeo.2005.06.031.

Ambrosi, C., and G. B. Crosta (2011), Valley shape influence on deformation mechanisms of rock slopes, *Geol. Soc. London Spec. Publ.*, *351*(1), 215–233, doi:10.1144/SP351.12.

Amitrano, D. (1999), Emission acoustique des roches et endommagement: Approches experimentale et numerique, application a la sismicite miniere, PhD thesis, Universite Joseph-Fourier - Grenoble I.

Amitrano, D. (2004), Emerging complexity in a simple model of the mechanical behaviour of rocks, *C. R. Geosci.*, *336*(6), 505–512, doi:10.1016/j.crte.2003.11.023.

Amitrano, D., and A. Helmstetter (2006), Brittle creep, damage, and time to failure in rocks, *J. Geophys. Res.*, *111*, B11201, doi:10.1029/2005JB004252.

Amitrano, D., J. R. Grasso, and G. Senfaute (2005), Seismic precursory patterns before a cliff collapse and critical point phenomena, *Geophys. Res. Lett.*, *32*, L08314, doi:10.1029/2004GL022270.

Anderson, O. L., and P. C. Grew (1977), Stress corrosion theory of crack propagation with applications to geophysics, *Rev. Geophys.*, *15*(1), 77–104, doi:10.1029/RG015i001p00077.

Atkinson, B. K. (1984), Subcritical crack growth in geological materials, *J. Geophys. Res.*, *89*(B6), 4077–4114, doi:10.1029/JB089iB06p04077.

Atkinson, B. K. (1987), *Fracture Mechanics of Rock*, Academic Press Inc., London.

Bachmann, D., S. Bouissou, and A. Chemenda (2004), Influence of weathering and pre-existing large scale fractures on gravitational slope failure: Insights from 3-D physical modelling, *Nat. Hazards Earth Syst. Sci.*, *4*, 711–717.

Bachmann, D., S. Bouissou, and A. Chemenda (2009), Analysis of massif fracturing during deep-seated gravitational slope deformation by physical and numerical modeling, *Geomorphology*, *103*(1), 130–135, doi:10.1016/j.geomorph.2007.09.018.

Ballantyne, C. K. (2002), Paraglacial geomorphology, *Quat. Sci. Rev.*, *21*(18-19), 1935–2017, doi:10.1016/S0277-3791(02)00005-7.

Ballantyne, C. K., and J. O. Stone (2004), The Beinn Alligin rock avalanche, NW Scotland: Cosmogenic 10 Be dating, interpretation and significance, *Holocene*, *14*(3), 448–453, doi:10.1191/0959683604hl720rr.

Baud, P., and P. Meredith (1997), Damage accumulation during triaxial creep of darley dale sandstone from pore volumometry and acoustic emission, *Int. J. Rock Mech. Min. Sci.*, *34*(3-4), 24.e1–24.e10, doi:10.1016/S1365-1609(97)00060-9.

Bhandari, R. (1988), Special lecture: Some practical lessons in the investigation and field monitoring of landslides, in *Proceedings of the 5th International Symposium on Landslides*, edited by C. Bonnard, pp. 1435–1457, A. A. Balkema, Rotterdam.

Boukharov, G., M. Chanda, and N. Boukharov (1995), The three processes of brittle crystalline rock creep, *Int. J. Rock Mech. Min. Sci. Geomech. Abstr.*, *32*(4), 325–335, doi:10.1016/0148-9062(94)00048-8.

Brantut, N., P. Baud, M. J. Heap, and P. G. Meredith (2012), Micromechanics of brittle creep in rocks, *J. Geophys. Res.*, *117*, B08412, doi:10.1029/2012JB009299.

Brantut, N., M. Heap, P. Meredith, and P. Baud (2013), Time-dependent cracking and brittle creep in crustal rocks: A review, *J. Struct. Geol.*, *52*, 17–43, doi:10.1016/j.jsg.2013.03.007.

Brideau, M.-A., M. Yan, and D. Stead (2009), The role of tectonic damage and brittle rock fracture in the development of large rock slope failures, *Geomorphology*, *103*(1), 30–49, doi:10.1016/j.geomorph.2008.04.010.

Bruckl, E., and M. Parotidis (2001), Estimation of large-scale mechanical properties of a large landslide on the basis of seismic results, *Int. J. Rock Mech. Min. Sci.*, *38*(6), 877–883, doi:10.1016/S1365-1609(01)00053-3.

Bruckl, E., and M. Parotidis (2005), Prediction of slope instabilities due to deep-seated gravitational creep, *Nat. Hazards Earth Syst. Sci.*, *5*(2), 155–172, doi:10.5194/nhess-5-155-2005.

Cai, M., P. Kaiser, H. Uno, Y. Tasaka, and M. Minami (2004), Estimation of rock mass deformation modulus and strength of jointed hard rock masses using the GSI system, *Int. J. Rock Mech. Min. Sci.*, *41*(1), 3–19, doi:10.1016/S1365-1609(03)00025-X.

Chemenda, A., T. Bois, S. Bouissou, and E. Tric (2009), Numerical modelling of the gravity-induced destabilization of a slope: The example of the la Clapiere landslide, southern france, *Geomorphology*, *109*(3-4), 86–93, doi:10.1016/j.geomorph.2009.02.025.

Cossart, E., R. Braucher, M. Fort, D. Bourles, and J. Carcaillet (2008), Slope instability in relation to glacial debuttressing in alpine areas (upper Durance catchment, southeastern France): Evidence from field data and 10 Be cosmic ray exposure ages, *Geomorphology*, *95*(1-2), 3–26, doi:10.1016/j.geomorph.2006.12.022.

Crosta, G., and A. Zanchi (2000), Deep seated slope deformations: Huge, extraordinary, enigmatic phenomena, in *Landslides in Research, Theory*

and Practice. Proceedings of the 8th International Symposium Landslides, Cardiff, June 2000, edited by E. Bromhead, N. Doxon, and M. Ibsen, pp. 351–358, Thomas Telford, London.

Crosta, G. B., and F. Agliardi (2003), Failure forecast for large rock slides by surface displacement measurements, *Can. Geotech. J.*, *191*(1), 176–191, doi:10.1139/T02-085.

Cruden, D., and X. Hu (1993), Exhaustion and steady state models for predicting landslide hazards in the Canadian Rocky Mountains, *Geomorphology*, *8*(4), 279–285, doi:10.1016/0169-555X(93)90024-V.

Eberhardt, E., D. Stead, and J. Coggan (2004), Numerical analysis of initiation and progressive failure in natural rock slopes—The 1991 Randa rockslide, *Int. J. Rock Mech. Min. Sci.*, *41*(1), 69–87, doi:10.1016/S1365-1609(03)00076-5.

Einstein, H., D. Veneziano, G. Baecher, and K. O'Reilly (1983), The effect of discontinuity persistence on rock slope stability, *Int. J. Rock Mech. Min. Sci. Geomech. Abstr.*, *20*(5), 227–236, doi:10.1016/0148-9062(83)90003-7.

Eisbacher, G. H. (1984), *Destructive Mass Movements in High Mountains: Hazard and Management*, Geological Survey of Canada, Ottawa.

El Bedoui, S., Y. Guglielmi, T. Lebourg, and J.-L. Perez (2009), Deep-seated failure propagation in a fractured rock slope over 10,000 years: The la Clapiere slope, the south-eastern French Alps, *Geomorphology*, *105*(3-4), 232–238, doi:10.1016/j.geomorph.2008.09.025.

Erismann, T. H., and G. Abele (2001), *Dynamics of Rockslides and Rockfalls*, Springer Berlin Heidelberg, New York.

Eslami, J., D. Grgic, and D. Hoxha (2010), Estimation of the damage of a porous limestone from continuous (*P*- and *S*-) wave velocity measurements under uniaxial loading and different hydrous conditions, *Geophys. J. Int.*, *183*(3), 1362–1375, doi:10.1111/j.1365-246X.2010.04801.x.

Forlati, F., G. Gioda, and C. Scavia (2001), Finite element analysis of a deep-seated slope deformation, *Rock Mech. Rock Eng.*, *34*(2), 135–159, doi:10.1007/s006030170019.

Griffiths, D. V., and P. A. Lane (1999), Slope stability analysis by finite elements, *Geotechnique*, *49*(3), 387–403.

Guglielmi, Y., and F. Cappa (2010), Regional-scale relief evolution and large landslides: Insights from geomechanical analyses in the Tinee valley (southern French Alps), *Geomorphology*, *117*(1-2), 121–129, doi:10.1016/j.geomorph.2009.11.016.

Gutiérrez-Santolalla, F., E. Acosta, S. Ríos, J. Guerrero, and P. Lucha (2005), Geomorphology and geochronology of sackung features (uphill-facing scarps) in the Central Spanish Pyrenees, *Geomorphology*, *69*(1-4), 298–314, doi:10.1016/j.geomorph.2005.01.012.

Hajiabdolmajid, V., P. Kaiser, and C. Martin (2002), Modelling brittle failure of rock, *Int. J. Rock Mech. Min. Sci.*, *39*(6), 731–741, doi:10.1016/S1365-1609(02)00051-5.

Heap, M., S. Vinciguerra, and P. Meredith (2009a), The evolution of elastic moduli with increasing crack damage during cyclic stressing of a basalt from Mt. Etna volcano, *Tectonophysics*, *471*(1-2), 153–160, doi:10.1016/j.tecto.2008.10.004.

Heap, M., P. Baud, P. Meredith, S. Vinciguerra, A. Bell, and I. Main (2011), Brittle creep in basalt and its application to time-dependent volcano deformation, *Earth Planet. Sci. Lett.*, *307*(1-2), 71–82, doi:10.1016/j.epsl.2011.04.035.

Heap, M. J., P. Baud, P. G. Meredith, A. F. Bell, and I. G. Main (2009b), Time-dependent brittle creep in Darley Dale sandstone, *J. Geophys. Res.*, *114*, B07203, doi:10.1029/2008JB006212.

Heap, M. J., D. R. Faulkner, P. G. Meredith, and S. Vinciguerra (2010), Elastic moduli evolution and accompanying stress changes with increasing crack damage: Implications for stress changes around fault zones and volcanoes during deformation, *Geophys. J. Int.*, *183*(1), 225–236, doi:10.1111/j.1365-246X.2010.04726.x.

Helmstetter, A., and S. Garambois (2010), Seismic monitoring of Séchilienne rockslide (French Alps): Analysis of seismic signals and their correlation with rainfalls, *J. Geophys. Res.*, *115*, F03016, doi:10.1029/2009JF001532.

Helmstetter, A., D. Sornette, J.-R. Grasso, J. V. Andersen, S. Gluzman, and V. Pisarenko (2004), Slider block friction model for landslides: Application to Vaiont and la Clapière landslides, *J. Geophys. Res.*, *109*, B02409, doi:10.1029/2002JB002160.

Hippolyte, J.-C., D. Bourles, R. Braucher, J. Carcaillet, L. Leanni, M. Arnold, and G. Aumaitre (2009), Cosmogenic 10 Be dating of a sackung and its faulted rock glaciers, in the Alps of Savoy (France), *Geomorphology*, *108*(3-4), 312–320, doi:10.1016/j.geomorph.2009.02.024.

Hoek, E., and E. Brown (1998), Practical estimates of rock mass strength, *Int. J. Rock Mech. Min. Sci.*, *34*(8), 1165–1186, doi:10.1016/S1365-1609(97)80069-X.

Hurlimann, M., A. Ledesma, J. Corominas, and P. C. Prat (2006), The deep-seated slope deformation at Encampadana, Andorra: Representation of morphologic features by numerical modelling, *Eng. Geol.*, *83*(4), 343–357, doi:10.1016/j.enggeo.2005.11.008.

Ishida, T., T. Kanagawa, and Y. Kanaori (2010), Source distribution of acoustic emissions during an in-situ direct shear test: Implications for an analog model of seismogenic faulting in an inhomogeneous rock mass, *Eng. Geol.*, *110*(3-4), 66–7 6, doi:10.1016/j.enggeo.2009.11.003.

Ivy-Ochs, S., H. Heuberger, P. W. Kubik, H. Kerschner, G. Bonani, M. Frank, and C. Schluchter (1998), The age of the Kofels event. Relative, 14C and cosmogenic isotope dating of an early holocene landslide in the central Alps (Tyrol, Austria), *Z. Gletscherkd. Glazialgeol.*, *34*, 57–68.

Ivy-Ochs, S., A. Poschinger, H.-A. Synal, and M. Maisch (2009), Surface exposure dating of the flims landslide, Graubunden, Switzerland, *Geomorphology*, *103*(1), 104–112, doi:10.1016/j.geomorph.2007.10.024.

Jaeger, J. C., and N. G. W. Cook (1976), *Fundamentals of Rock Mechanics,* 2nd ed., Champman and Hall, London.

Kachanov, M. (1993), Elastic solids with many cracks and related problems, in *Advances in Applied Mechanics*, edited by J. Hutchinson and T. Wu, pp. 256–426, Academic Press, London.

Kasperski, J. (2008), Confrontation des donnees de terrain et de l'imagerie multi-sources pour la comprehension de la dynamique des mouvements de versants, PhD thesis, Universite Claude Bernard.

Katz, O., and Z. Reches (2004), Microfracturing, damage, and failure of brittle granites, *J. Geophys. Res.*, *109*, B01206, doi:10.1029/2002JB001961.

Kemeny, J., and N. Cook (1986), Effective moduli, non-linear deformation and strength of a cracked elastic solid, *Int. J. Rock Mech. Min. Sci. Geomech. Abstr.*, *23*(2), 107–118, doi:10.1016/0148-9062(86)90337-2.

Kennedy, B., and K. Niemeyer (1971), *Slope Monitoring Systems Used in the Prediction of a Major Slope Failure at the Chuquicamata Mine, Chile*, pp. 215–225, Blakeme, Johannesburg, Rotterdam.

Kranz, R. L., and C. H. Scholz (1977), Critical dilatant volume of rocks at the onset of tertiary creep, *J. Geophys. Res.*, *82*(30), 4893–4898, doi:10.1029/JB082i030p04893.

Kranz, R. L., W. J. Harris, and N. L. Carter (1982), Static fatigue of granite at 200∘C, *Geophys. Res. Lett.*, *9*(1), 1–4, doi:10.1029/GL009i001p00001.

Kulatilake, P. H. S. W., J. Park, and J.-g. Um (2004), Estimation of rock mass strength and deformability in 3-D for a 30 m cube at a depth of 485 m at Äspö hard rock laboratory, *Geotech. Geol. Eng.*, *22*(3), 313–330, doi:10.1023/B:GEGE.0000025033.21994.c0.

Kveldsvik, V., A. M. Kaynia, F. Nadim, R. Bhasin, B. Nilsen, and H. H. Einstein (2009), Dynamic distinct-element analysis of the 800 m high Aknes rock slope, *Int. J. Rock Mech. Min. Sci.*, *46*(4), 686–698, doi:10.1016/j.ijrmms.2008.10.007.

Le Roux, O., S. Schwartz, J. F. Gamond, D. Jongmans, D. Bourles, R. Braucher, W. Mahaney, J. Carcaillet, and L. Leanni (2009), CRE dating on the head scarp of a major landslide (Sechilienne, french Alps), age constraints on Holocene kinematics, *Earth Planet. Sci. Lett.*, *280*(1-4), 236–245, doi:10.1016/j.epsl.2009.01.034.

Main, I. G. (2000), A damage mechanics model for power-law creep and earthquake aftershock and foreshock sequences, *Geophys. J. Int.*, *142*(1), 151–161, doi:10.1046/j.1365-246x.2000.00136.x.

McCalpin, J. (1999), *Criteria for Determining the Seismic Significance of Sackungen and Other Scarplike Landforms in Mountainous Regions*, pp. 122–142, US Nuclear Regulatory Commission, Washington, D. C.

McCleary, J., United Engineers & Constructors, Inc., and Washington Public Power Supply System (1978), *Straight Creek Fault Zone Study: 1872 Earthquake Studies: Washington Public Power Supply System: Nuclear Projects no. 1 and 4*, Woodward-Clyde Consultants, San Francisco, California.

Min, K.-B., and L. Jing (2003), Numerical determination of the equivalent elastic compliance tensor for fractured rock masses using the distinct element method, *Int. J. Rock Mech. Min. Sci.*, *40*(6), 795–816, doi:10.1016/S1365-1609(03)00038-8.

Monjuvent, G., and J. Winistorfer (1980), *Glaciations Quaternaires Dans Les Alpes Franco-Suisses et Leur Piedmont*, (Livret-guide; G26), excursion 099 ed., International Geological Congress, France.

Muller, J. R., and S. J. Martel (2000), Numerical models of translational landslide rupture surface growth, *Pure Appl. Geophys.*, *157*(6-8), 1009–1038, doi:10.1007/s000240050015.

Nara, Y., N. Hiroyoshi, T. Yoneda, and K. Kaneko (2010), Effects of relative humidity and temperature on subcritical crack growth in igneous rock, *Int. J. Rock Mech. Min. Sci.*, *47*(4), 640–646, doi:10.1016/j.ijrmms.2010.04.009.

Newmark, N. M. (1965), Effects of earthquakes on dams and embankments, *Geotechnique*, *15*(2), 139–159.

Nishii, R., and N. Matsuoka (2010), Monitoring rapid head scarp movement in an alpine rockslide, *Eng. Geol.*, *115*(1-2), 49–57, doi:10.1016/j.enggeo.2010.06.014.

Petley, D. N., M. H. Bulmer, and W. Murphy (2002), Patterns of movement in rotational and translational landslides, *Geology*, *30*(8), 719–722, doi:10.1130/0091-7613(2002)030<0719:POMIRA>2.0.CO;2.

Petley, D. N., T. Higuchi, D. J. Petley, M. H. Bulmer, and J. Carey (2005), Development of progressive landslide failure in cohesive materials, *Geology*, *33*(3), 201–204, doi:10.1130/G21147.1.

Potherat, P., and L. Effendiantz (2009), Neotectonique et grands mouvements de versant. le cas de Sechilienne (Isere, France), *Bull. Eng. Geol. Environ.*, *68*(4), 567–577, doi:10.1007/s10064-009-0221-2.

Prager, C., S. Ivy-Ochs, M. Ostermann, H.-A. Synal, and G. Patzelt (2009), Geology and radiometric ^{14}C-, ^{36}Cl- and Th-/U-dating of the Fernpass rockslide (Tyrol, Austria), *Geomorphology*, *103*(1), 93–103, doi:10.1016/j.geomorph.2007.10.018.

Saito, M., and H. Uezawa (1961), Failure of soil due to creep, in *Proceedings of the 5th International 'Conference on Soil Mechanics and Foundation Engineering, Paris,* vol. 1, edited by Ed. Dunod, pp. 315–318, Montreal.

Sanchez, G., Y. Rolland, M. Corsini, R. Braucher, D. Bourlès, M. Arnold, and G. Aumaître (2010), Relationships between tectonics, slope instability and climate change: Cosmic ray exposure dating of active faults, landslides and glacial surfaces in the SW alps, *Geomorphology*, *117*(1-2), 1–13, doi:10.1016/j.geomorph.2009.10.019.

Sano, O., and Y. Kudo (1992), Relation of fracture resistance to fabric for granitic rocks, *Pure Appl. Geophys.*, *138*(4), 657–677, doi:10.1007/BF00876343.

Sethna, J. P., K. A. Dahmen, and C. R. Myers (2001), Crackling noise, *Nature*, *410*(6825), 242–250, doi:10.1038/35065675.

Soldati, M., A. Corsini, and A. Pasuto (2004), Landslides and climate change in the Italian Dolomites since the late glacial, *Catena*, *55*(2), 141–161, doi:10.1016/S0341-8162(03)00113-9.

Stead, D., E. Eberhardt, and J. S. Coggan (2006), Developments in the characterization of complex rock slope deformation and failure using numerical modelling techniques, *Eng. Geol.*, *83*(1-3), 217–235, doi:10.1016/j.enggeo.2005.06.033.

Strozzi, T., R. Delaloye, A. Kaab, C. Ambrosi, E. Perruchoud, and U. Wegmuller (2010), Combined observations of rock mass movements using satellite SAR interferometry, differential GPS, airborne digital photogrammetry, and airborne photography interpretation, *J. Geophys. Res.*, *115*, F01014, doi:10.1029/2009JF001311.

Tarchi, D., N. Casagli, S. Moretti, D. Leva, and A. J. Sieber (2003), Monitoring landslide displacements by using ground-based synthetic aperture radar interferometry: Application to the Ruinon landslide in the Italian Alps, *J. Geophys. Res.*, *108*(B8), 2387, doi:10.1029/2002JB002204.

Tinner, W., P. Kaltenrieder, M. Soom, P. Zwahlen, M. Schmidhalter, A. Boschetti, and C. Schluchter (2005), The postglacial rockfall in the kander valley (Switzerland): Age and effects on palaeoenvironments, *Eclogae Geol. Helv.*, *98*(1), 83–95, doi:10.1007/s00015-005-1147-8.

Van Asch, T. W. J. V., J.-P. Malet, L. P. H. V. Van Beek, and D. Amitrano (2007), Techniques, issues and advances in numerical modelling of landslide hazard, *Bull. Soc. Geol. Fr.*, *178*(2), 65–88, doi:10.2113/gssgfbull.178.2.65.

Varnes, D. J., D. H. Radbruch-Hall, and W. Z. Savage (1989), Topographic and Structural Conditions in Areas of Gravitational Spreading of Ridges in the Western United States, *United States Geological Survey*, *1496*, 1–28.

Vengeon, J., A. Giraud, P. Antoine, and L. Rochet (1999), Contribution l'analyse de la formation et de la rupture des grands versants rocheux en terrain cristallophyllien, *Can. Geotech. J.*, *36*, 1123–1136.

Voight, B. (1989), A relation to describe rate-dependent material failure, *Science*, *243*(4888), 200–203, doi:10.1126/science.243.4888.200.

Wassermann, J., G. Senfaute, D. Amitrano, and F. Homand (2009), Evidence of dilatant and non-dilatant damage processes in oolitic iron ore: *P*-wave velocity and acoustic emission analyses, *Geophys. J. Int.*, *177*(3), 1343–1356, doi:10.1111/j.1365-246X.2008.04017.x.

Zapperi, S., A. Vespignani, and H. E. Stanley (1997), Plasticity and avalanche behaviour in microfracturing phenomena, *Nature*, *388*(6643), 658–660.

Zvelebill, J., and M. Moser (2001), Monitoring based time-prediction of rock falls: Three case-histories, *Phys. Chem. Earth, Part B*, *26*(2), 159–167, doi:10.1016/S1464-1909(00)00234-3.